International Journal of Solids and Structures 51 (2014) 3042–3057

Contents lists available at ScienceDirect

International Journal of Solids and Structures

journal homepage: www.elsevier.com/locate/ijsolstr

Mechanics and full-field deformation study of the Ring Hoop Tension Test

Chris P. Dick, Yannis P. Korkolis *

Department of Mechanical Engineering, University of New Hampshire, 33 Academic Way, Durham, NH 03824, USA

ARTICLE INFO

Article history:
Received 26 December 2013
Received in revised form 27 April 2014
Available online 9 May 2014

Keywords:
Anisotropy
Experimental techniques
Tube forming
Aluminum alloys
Digital Image Correlation

ABSTRACT

We investigate the mechanics of the Ring Hoop Tension Test (RHTT), as a means to assess the properties of anisotropic tubes in the hoop direction. This test involves placing a ring extracted from the tube over two close-fitting D-shaped mandrels that are then parted using a universal testing machine. Since the curvature of the ring does not change during loading, the ring undergoes only stretching. We determine the effects of contact pressure, radial stress, and friction between the tube and mandrels using FEA simulations. The effects of the pre-existing thickness eccentricity and of the specimen-making procedure on the recorded RHTT response are also assessed with a combination of experiments and analysis. We tested tubes from Al-6061-T4 with a diameter/thickness ratio of 20. We found that as the friction increases beyond 0.1–0.15, the state of uniaxial tension is deteriorated, indicating that care must be taken to minimize the tube-mandrel friction. We determined that although these tubes have a relatively large thickness eccentricity (±4% of the nominal thickness), this had no effect on the recorded results. We showed that the tubes should not be turned to remove that eccentricity, as the machining process induces damage that is noticeable in the results. We found that the contact pressure and the contact-induced radial stress cause limited deviations from uniaxial tension, comparable to the case of a tube under axial load and internal pressure which is often used for assessing the material properties in the hoop direction. Central in our analyses is the knowledge of the hoop strain field, which was assessed using 3D Digital Image Correlation. We propose a data reduction procedure for RHTT that accounts for all the above effects. Finally, with all effects accounted for, we establish the anisotropy of the extruded Al-6061-T4 tubes studied.

1. Introduction

Reliable numerical simulations of material forming processes require accurate models of the material behavior, including plastic flow, anisotropy and failure. There is significant body of knowledge that indicates that accurate material models are imperative for numerical predictions of failure that match experimental observations (e.g., see Kuwabara et al., 2011). In the case of metal sheets, a large variety of experimental techniques have been devised to calibrate anisotropic material models (Kuwabara, 2007). However, when the workpiece is in tubular form, many of these techniques are inapplicable.

Fig. 1 shows a variety of testing techniques available for materials in tubular form (Kim et al., accepted for publication). The simplest way of assessing the hoop properties (plastic flow anisotropy and failure) is shown in Fig. 1a: an arc is extracted from the tube, flattened and then tested in uniaxial tension (see the ASTM E-8 standard, ASTM, 2008). Since the flattening introduces a prestrain on the specimen, this method can only be used for qualitative studies of the hoop response, or for assessing the weld strength of electric-resistance-welded (ERW) tubes. Another simple technique is tube-end flaring (Daxner et al., 2005), shown in Fig. 1b. In this method, a cone is driven coaxially with the tube, which expands to accommodate the cone movement. While at first approximation the end of the tube can be considered to experience uniaxial tension, the presence of the friction often leads to multiple necking in the circumference. Hence the failure limits determined from this test may not correspond to pure hoop tension. The classic experiment to assess the hoop properties is the inflation of a tube under axial load and internal pressure (Korkolis and Kyriakides, 2008, 2009; Korkolis et al., 2010; Kuwabara et al., 2005; Kuwabara and Sugawara, 2013), shown in Fig. 1c. While this experiment has been used extensively in plasticity, it requires relatively complex testing equipment. In contrast, the Ring Hoop Tension Test (RHTT) shown in Fig. 1d only requires a universal testing

* Corresponding author. Tel.: +1 603 862 2772.
E-mail address: yannis.korkolis@unh.edu (Y.P. Korkolis).

http://dx.doi.org/10.1016/j.ijsolstr.2014.04.023
0020-7683/

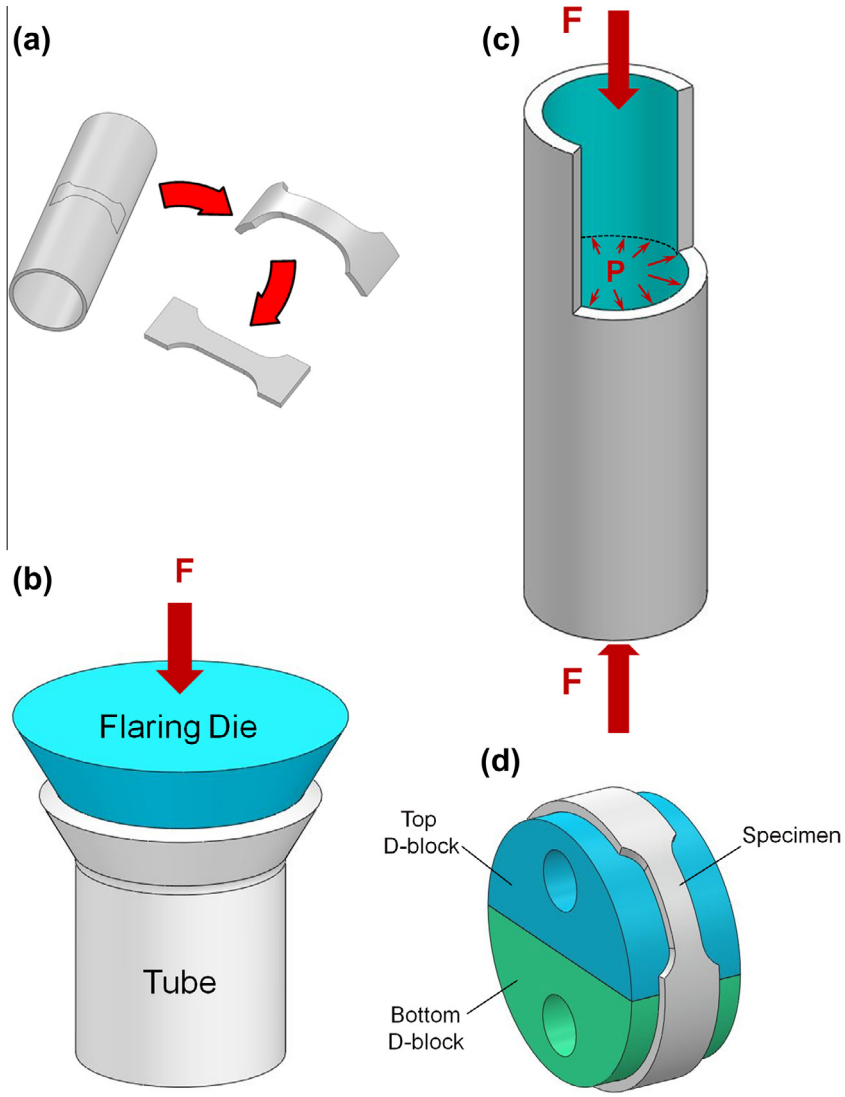

Fig. 1. Testing methods for assessing the plastic flow and failure properties of tubes in the hoop direction. (a) Flattening and tension test, (b) tube flaring, (c) tube inflation under axial load and internal pressure and, (d) Ring Hoop Tension Test (RHTT).

machine. In that test, a dogbone specimen geometry is machined on a ring extracted from the tube. The ring is then placed over two closely-fitting D-shaped mandrels that are parted with the use of a testing machine. Since the curvature of the ring does not change during testing, the specimen undergoes only stretching and no bending.

The RHTT technique was proposed about 15 years ago. Arsene and Bai (1996, 1998) used various combinations of internal mandrels to stretch a ring without inducing bending. They used finite element analysis to investigate certain factors of this test such as the effect of friction on the response and compared the analysis to their experiments. Their work was directed towards nuclear fuel cladding applications and the materials examined were an Al–Si alloy and Zircalloy. Wang et al. (2002) examined the RHTT of a steel tube for hydroforming applications. The average hoop strain was measured with an extensometer during the test. They also used circle-grid analysis for assessing the spatial distribution of the strains after the end of the test. He et al. (2010) used the RHTT to study the warm formability of AZ 31B magnesium tubes for hydroforming applications. Note that the RHTT readily lends itself to high-temperature testing due to its simplicity. Link et al. (1998) also looked at the effects of high temperature deformation along with strain-rate effects, but used a wider RHTT specimen to impose plane-strain conditions. They used that geometry to study the failure of Zircalloy cladding for nuclear fuel applications. Walsh and Adams (2008) used an arrangement of 4 internal quadrant mandrels to stretch composite rings, but found this fixture arrangement to be difficult to work properly. Finally, Korkolis et al. (2013) presented a preliminary experimental investigation of RHTT using a full-field Digital Image Correlation method to assess the evolution of the strain field during the RHTT.

In this paper, we examine the Ring Hoop Tension Test in an effort to establish its validity, as well as determine a standardized testing procedure that can yield reliable and repeatable results. We selected to study the behavior of a relatively thick-walled (diameter/thickness = 20) extruded tube, to accentuate the effects of wall thickness and its circumferential variation on the response. We begin with a simple analytical model, which illustrates the effect of friction on the performance of the test. A more complete, 3D finite element model of the RHTT is then considered. This model is probed to determine the effects of the contact pressure, the thickness eccentricity and the data reduction technique on the accuracy of the RHTT results. It is also used to help in determining the appropriate RHTT specimen geometry. Guided by these results,

the second part of the paper deals with the RHTT experiments. We use 3D Digital Image Correlation to assess and explain the non-uniformity of the strain field. We also quantitatively determine the coefficient of friction and the effect of specimen-making on the recorded responses. With the problem dissected and decoupled in this way, we arrive at the flow curve of the material in the hoop direction and hence establish its anisotropy.

2. Analytical and numerical investigation

2.1. Analytical modeling

A very simple analytical model, which in essence is the belt equation (or Eytelwein's formula) from statics, will be used to shed light at the distribution of the internal force in the hoop direction in terms of the friction coefficient between the ring and the rigid mandrel. (For an alternative approach, see He et al., 2008.) Consider a thin ring wrapped around a rigid, rough circular arc and pulled by a pair of tangential forces (Fig. 2a). Since the curvature remains constant, both the shear force and the bending moment are zero, i.e., the ring undergoes stretching only. This observation forms the basis of the RHTT. However, due to the presence of friction a major concern in the RHTT is whether the axial force is uniformly distributed in the hoop direction. Denoting the axial force $N(\theta)$ and the contact pressure $p(\theta)$ and considering the radial and hoop equilibrium of a differential element of the ring (Fig. 2b), it is easily shown for the internal force that:

$$N(\theta) = N(0)e^{-\mu\theta} \tag{1}$$

and for the contact pressure that:

$$p(\theta) = \frac{N(\theta)}{R} \tag{2}$$

A plot of Eq. (1) considering a quarter-circle arc is given in Fig. 3. The internal force can vary significantly along the circumference of the tube at large values of the friction. However, for the quarter-circle arc the internal force $N(90)$ equals $0.92 \times N(0)$ for $\mu = 0.05$ and $0.85 \times N(0)$ for $\mu = 0.1$, respectively. Furthermore, in the latter case the internal force varies less than 5% along an arc from 30° to 60°.

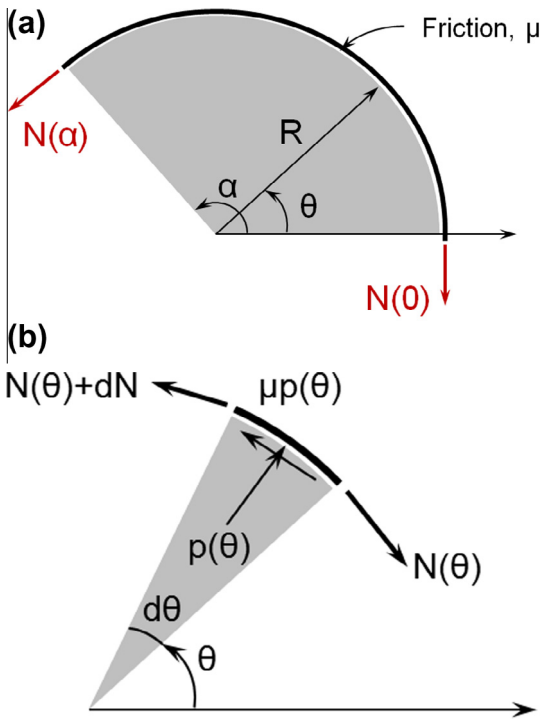

Fig. 2. For the derivation of the analytical model of RHTT. (a) Section of specimen and, (b) differential element.

2.2. Finite element modeling

The analytical model described offers a first glimpse of the mechanics of the RHT-Test. To gain a more complete understanding of the experiment, a finite element model was created in the nonlinear implicit code Abaqus/Standard. From preliminary experiments it was determined that a gage-length-to-thickness aspect ratio of eight would be the best for the RHTT specimens (see Section 3). Taking advantage of the symmetries present, only half of the specimen was simulated. The model was meshed with solid linear elements with reduced integration (C3D8R), arranged in the mesh of Fig. 4a, which was arrived at after suitable parametric studies (Dick, 2014). Five elements were used through the thickness, while the circumferential density of the mesh was increased in the gage-section of the specimen. The use of linear elements was dictated by the presence of contact. Three models were created: one with a uniform thickness and two with thickness eccentricity, which is sometimes noticeable in extruded tubes. Two relatively large eccentricities (±4% and ±10% of the nominal thickness) were considered here, with the thickness varying as a sine function of the arc. The D-shaped mandrels (or D-blocks) were represented by analytical rigid shells (Anon, 2012). Surface-to-surface contact was used with a no-penetration normal behavior ("hard" contact) and a friction coefficient of 0.01. This friction coefficient was chosen to keep the friction low to avoid the effects discussed in Section 2.1. The material model adopted for this study was the rate-independent J_2 flow theory of plasticity with isotropic hardening and an associated flow rule. The work-hardening curve of Al-6061-T4 determined in Section 3.1 from strips extracted along the tube axis was used. The two nodes identified in Fig. 4a as "Ext1" and "Ext2" were selected to represent the extensometer, while a reference point on the top D-block (RP1) was monitored to represent the load cell of the testing machine. Note that the strains reported here were converted from the change-of-cord measurements of the extensometer to change-of-circumference. The simulation was run in two steps: in the first, the small initial gap between the D-blocks and ring was closed by displacing both D-blocks. In the second, the top D-block was held in place and the bottom D-block was displaced vertically downwards, replicating the operation of the testing machine used for the experiments.

Fig. 4b shows the hoop stress distribution in the uniform ring for a corresponding hoop strain of 8.5%. Notice that the hoop stress is uniform in the gauge section, while outside it remains close to the proportional stress of the material (which is 87 MPa, see Section 3). The two segments of the ring that are between the two parting D-blocks are experiencing combined unbending and stretching, which is visible in Fig. 4b.

A concern regarding the validity of RHTT is that the contact pressure and the contact-induced radial stresses affect the response of the material. The numerical model was used to probe the contact pressure between the uniform ring and the D-block, as well as the resulting radial stress. The contact pressure on the inside surface of the ring is shown on the model in Fig. 5a (taken at the same instance as the hoop stress shown in Fig. 4b) and its evolution is plotted over the contact area, for various levels of hoop strain, in Fig. 5b. The instances that the contact pressure was output are identified on the stress–strain curve of Fig. 5c. They were intentionally chosen to correspond to elastic, small plastic and large plastic deformation of the specimen. Returning to Fig. 5b, it can be seen that the contact pressure is fairly constant in the gage-section, not unlike the fluid pressure in a tube inflation

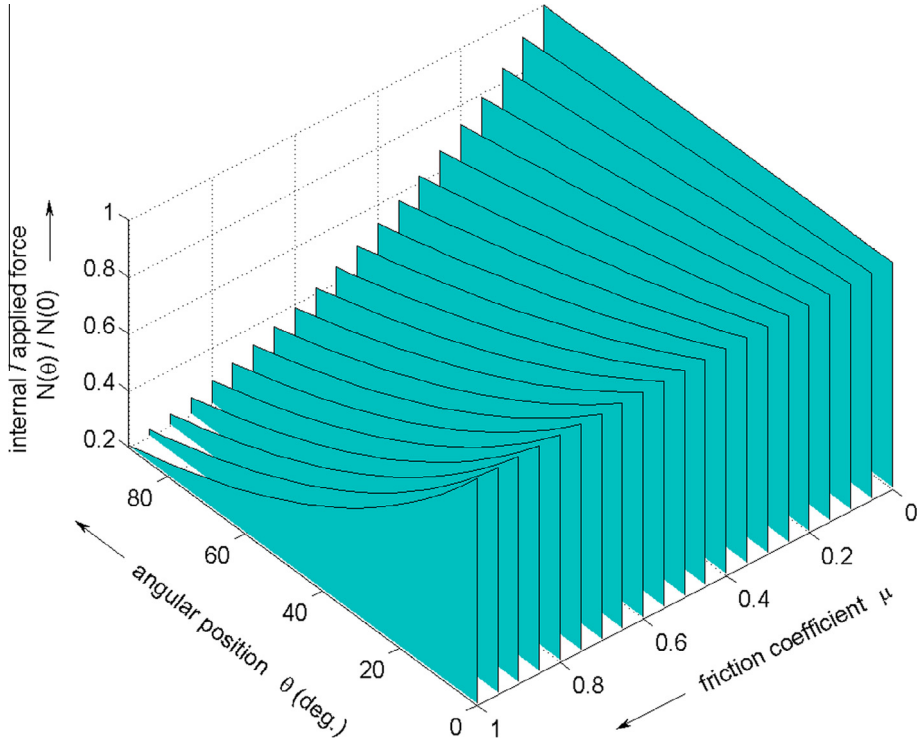

Fig. 3. Variation of the internal force along the arc in terms of the ring-mandrel friction coefficient.

experiment. Interestingly, the ratio of the contact pressure to the hoop stress remains about 1:10 throughout the deformation, which is the same as the thickness/radius ratio for the tube considered, as in an inflation experiment.

The corresponding radial stress evolution was monitored at 4 locations within the gage-section. These are identified as A–D in Fig. 6a and were selected to represent "random" locations within the gage-section of the uniform ring, with "A" closer to the free surface and "D" closer to the contact interface. At each θ and z location, the radial stress at the 5 integration points available through the thickness were monitored throughout the simulation up until the onset of necking. The results, normalized with the corresponding hoop stress at each of these points, are shown in Fig. 6b–e. It can be seen that in every position, the radial stress does not exceed 8% of the hoop stress. Furthermore, this ratio is for the integration points closest to the contact interface, while those farther away exhibit ratios below 6%.

The variation of the radial and the axial stress through the thickness of the gage-section at location C (Fig. 6a) for different levels of loading is shown in Fig. 7a and b. The radial stress starts from a value equal to the contact pressure and dies out to zero at the free surface. (Notice that the data is extracted at the 5 integration points available through the thickness, so there is no data on the contact interface and on the free surface themselves.) While the ring is still elastic, the radial stress is seen to be nonlinear, while soon after yielding it appears to vary linearly through the thickness. We noticed in the simulations that the radial stress does not vary as $\sim 1/r^2$ in the elastic case and $\sim \ln(r/a)$ in the plastic case, indicating a departure of this problem from the classical solution (e.g., Kachanov, 2004) of the elastoplastic thick-walled tube under internal pressure. The axial stress beyond yielding remains limited (less than 5% of the corresponding hoop).

As a result of the mild radial and axial stresses that develop, a plot of the hoop and the equivalent stresses vs. the plastic strain (hoop and equivalent, respectively) for the locations identified in Fig. 6a as A–D reveals that the hoop stress can approximate the uniaxial material behavior quite well (see Fig. 8a). As a further check, the development of the equivalent plastic strain at these 4 locations is presented in Fig. 8b, along with the average response as would be recorded by an extensometer spanning the gage-section. As before, the deviation between the responses from the 4 locations and the average one ranges from small to negligible.

The negligible effect of the eccentricity on the hoop stress–strain response is presented in Fig. 9. The hoop stress was computed by taking the force monitored through the simulation at the reference point RP1 in Fig. 4a and dividing it by the initial cross-sectional area of the gage-section. For the case of the eccentric simulations, the average initial cross-sectional area of the gage-section was used in the hoop stress calculation.

The eccentric responses are seen to follow the one from the uniform finite element model almost exactly, so that the eccentricity has a minimum effect on the flow response. In addition, it can be seen that all three responses closely approximate the input stress–strain curve, which serves as a further validation of the RHTT. However, the ultimate tensile stress and the corresponding uniform strain are sensitive to the eccentricity. This implies that if the RHTT is used to probe failure in addition to plastic flow anisotropy, care must be taken in interpreting the data from eccentric tubes.

3. Ring hoop tension experiments

The experiments were performed on Al-6061-T4 tubes of 60 mm outside diameter and 3 mm nominal thickness. The tubes were extruded from a solid billet through a porthole die (e.g., Lange, 1985), which resulted in 3 cold-welds running along the axis of the tube. Fig. 10a shows a schematic of the tube, while Fig. 10b shows an optical micrograph of the three cold-welded regions. The welds were exposed by etching a polished specimen using Keller's reagent. It can be seen that the cold-welding affects the tube microstructure only locally, although the welds are not

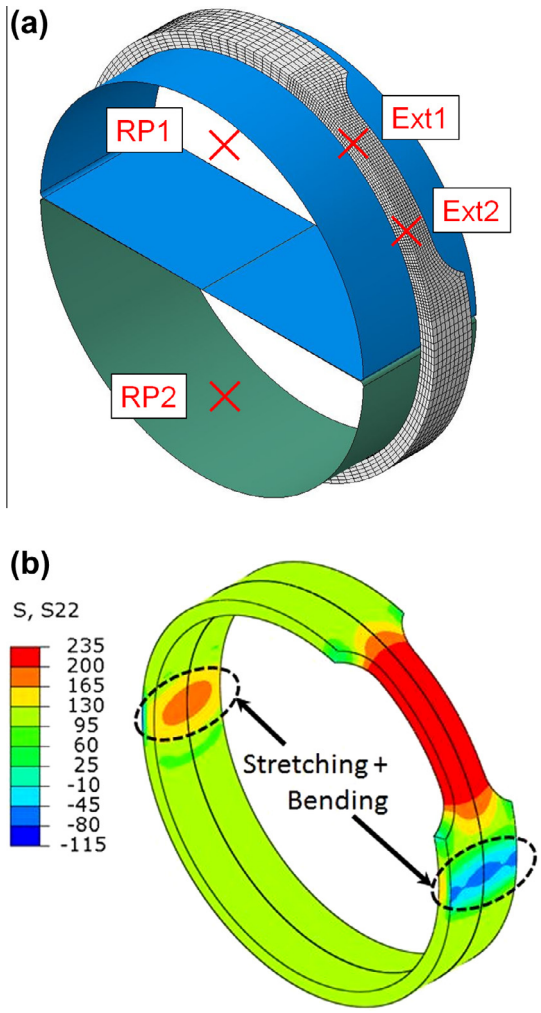

Fig. 4. (a) Finite element model of RHTT, showing the symmetry invoked and the nodal locations used for the extensometer and the two reference points. (b) Finite element prediction of the hoop stress (units: MPa).

strictly radial. At any rate, the disturbance is limited to a very narrow arc in the tube circumference (less than 5° each). Since the tubes were extruded, they exhibited a relatively large thickness eccentricity (±4% of the nominal thickness), shown in Fig. 10c. This value was adopted in the numerical investigation of Section 2.2 above. Lastly, marked in Fig. 10c is the location of the 3 welds. While they trisect the circumference, the arcs between them are not exactly 120°, presumably due to the tolerances of the porthole die.

3.1. Material characterization from tension tests on strips

The mechanical properties of the Al-6061-T4 tubes in the axial direction were evaluated by extracting tensile specimens as shown in Fig. 10a. The specimen geometry followed the ASTM E-8 standard (subsize geometry). The specimens were CNC-machined from the tubes in both the base and weld areas to determine if these different sections exhibit a different response. In addition to distinguishing tests between base and weld sections, the weld specimens were separated into three groups, one for each specific weld line. These weld groupings were called A, B, and C and kept constant throughout the testing.

The experiments were performed under displacement control on a 250 kN servohydraulic testing machine (MTS Landmark 370 with a Flextest 40 controller and the MTS 793 data acquisition and control software), equipped with hydraulic wedge grips (model MTS 647). The displacement rate of the actuator was set to 25.4×10^{-3} mm/s to correspond to quasistatic testing; indeed, the strain-rate measured was 7×10^{-4}/s. The strain was acquired during testing using a mechanical extensometer (MTS 634.12E–24). In addition, three-dimensional Digital Image Correlation (DIC) was used in some of the experiments to acquire the full strain-field and its evolution during loading. The DIC system used was VIC-3D from Correlated Solutions, Inc. Two 2.0 Megapixel digital cameras (Point Grey Research, Inc.) with 35 mm Schneider lens were used.

Tension testing of strips extracted from tubes oftentimes presents difficulties, as the gripping flattens the specimens and can induce problematic deformation behavior, such as changing of the curvature in the gage-section during the testing, curling of the strip on itself, premature localization as a result of that, etc. In this investigation, the shoulder of the strip specimens was 10 mm (following the ASTM E-8 standard), while the tube thickness was 3 mm. Hence the cross-section had an almost 3-to-1 aspect ratio and the curvature of the strips was barely noticeable, so that such complications were avoided.

The axial stress–strain responses of the base and weld material specimens are given in Fig. 11a and b. Up to the maximum load (UTS) the responses show some specimen-to-specimen variation, while the post-UTS tails have much more scatter, as usual. Average curves for both the base and weld material specimens were calculated and can be seen as the cyan curves in Fig. 11a and b. (Notice that the post-UTS average curve shown does not have a physical meaning.) It is interesting to see that each weld area appears to have its own response, shown by the grouping of the A, B and C specimen responses in Fig. 11c, which is a close-up of Fig. 11b. This observation can be possibly attributed to the manufacturing tolerances of the porthole extrusion die, which may have led to slightly different amounts of work-hardening for each cold weld during tube-making. Finally, the averaged responses from Fig. 11a and b are shown in Fig. 12. As perhaps expected, the presence of the weld line has little effect when the loading is applied along that line. These curves will be used in the rest of this work as representative of the axial response of the material.

The evolution of the axial strain during testing and the development of the deformation localization were probed with the DIC system and are shown in Fig. 13a and b. The axial strain was extracted along the gage-section at increasing levels of overall average strain, identified on the stress–strain curve (Fig. 13a) as green squares. The strain evolution is plotted in Fig. 13b, showing the typical behavior of a localization problem. While the deformation is uniform, the local values of the nominal strain match the average imposed strain very closely. The deformation then localizes in a diffuse neck, which stretches further until the specimen fails. For the present material, the neck extends for about 1/5 of the original gage-section length, or, in other words, it is comparable to the thickness of the specimen. Note that the DIC system provides the Lagrangian strain, which is then easily converted (for this uniaxial stress state) to nominal strain. However, the post-necking results are only approximately correct (Cullen and Korkolis, 2013).

To establish the strain-rate dependence of the material, an abrupt strain-rate change-, or jump-test was performed (Hosford and Caddell, 2007) on a specimen from the base material. The strain-rate during this test was varied five times in the order: 7×10^{-4}, 7×10^{-3}, 3.3×10^{-4}, 3.3×10^{-2}, and 8×10^{-4}/s. The result is plotted in Fig. 14, along with the base and weld material average axial stress–strain responses. It can be claimed that the material is not rate-sensitive in the strain-rate range examined.

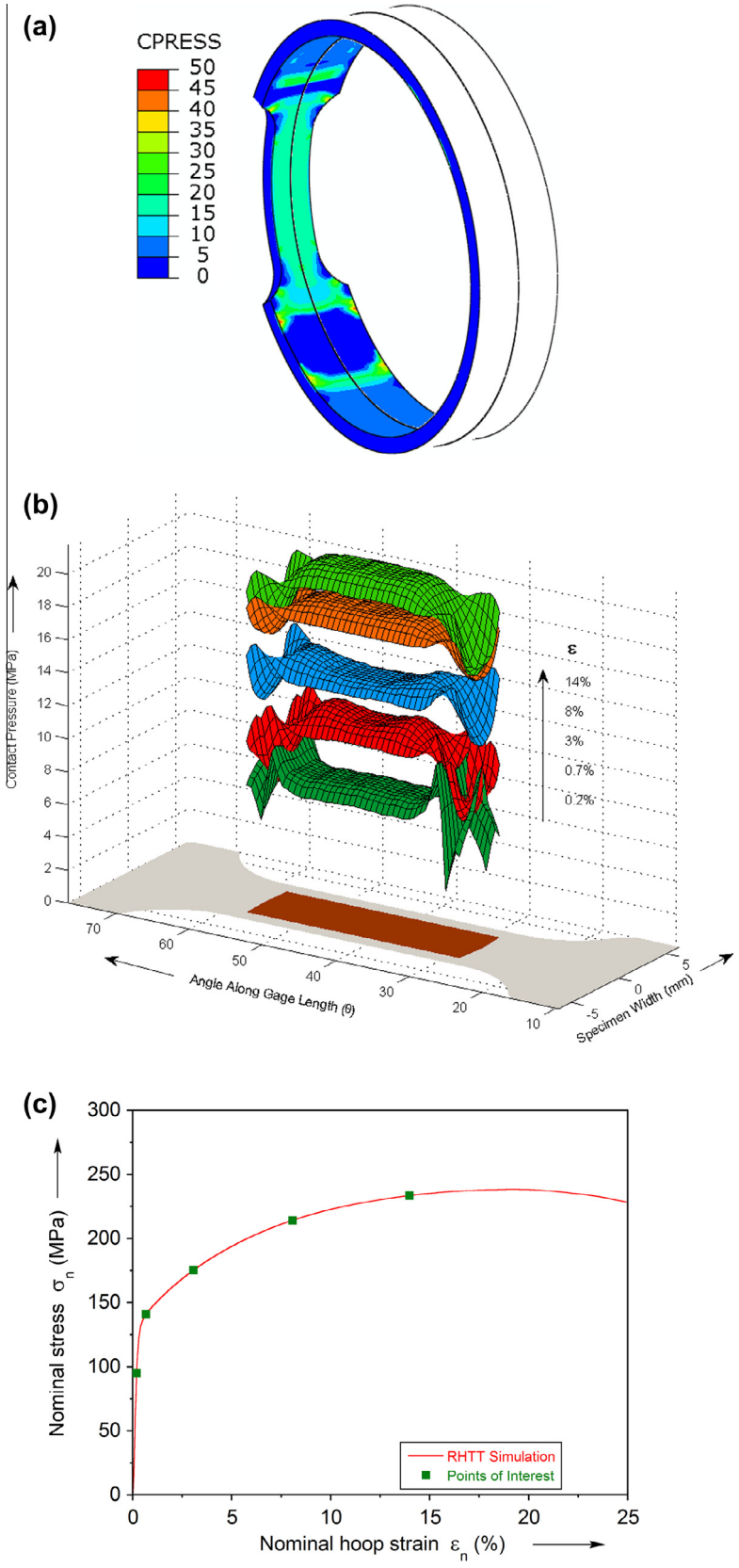

Fig. 5. (a) Finite element predictions of the contact pressure (units: MPa) between the specimen and the D-shaped mandrels. (b) Variation of the contact pressure along a patch in the gage-section (highlighted in dark red) at various levels of average hoop strain. (c) Instances along the simulation when the data of (b) was extracted. (For interpretation of the references to color in this figure legend, the reader is referred to the web version of this article.)

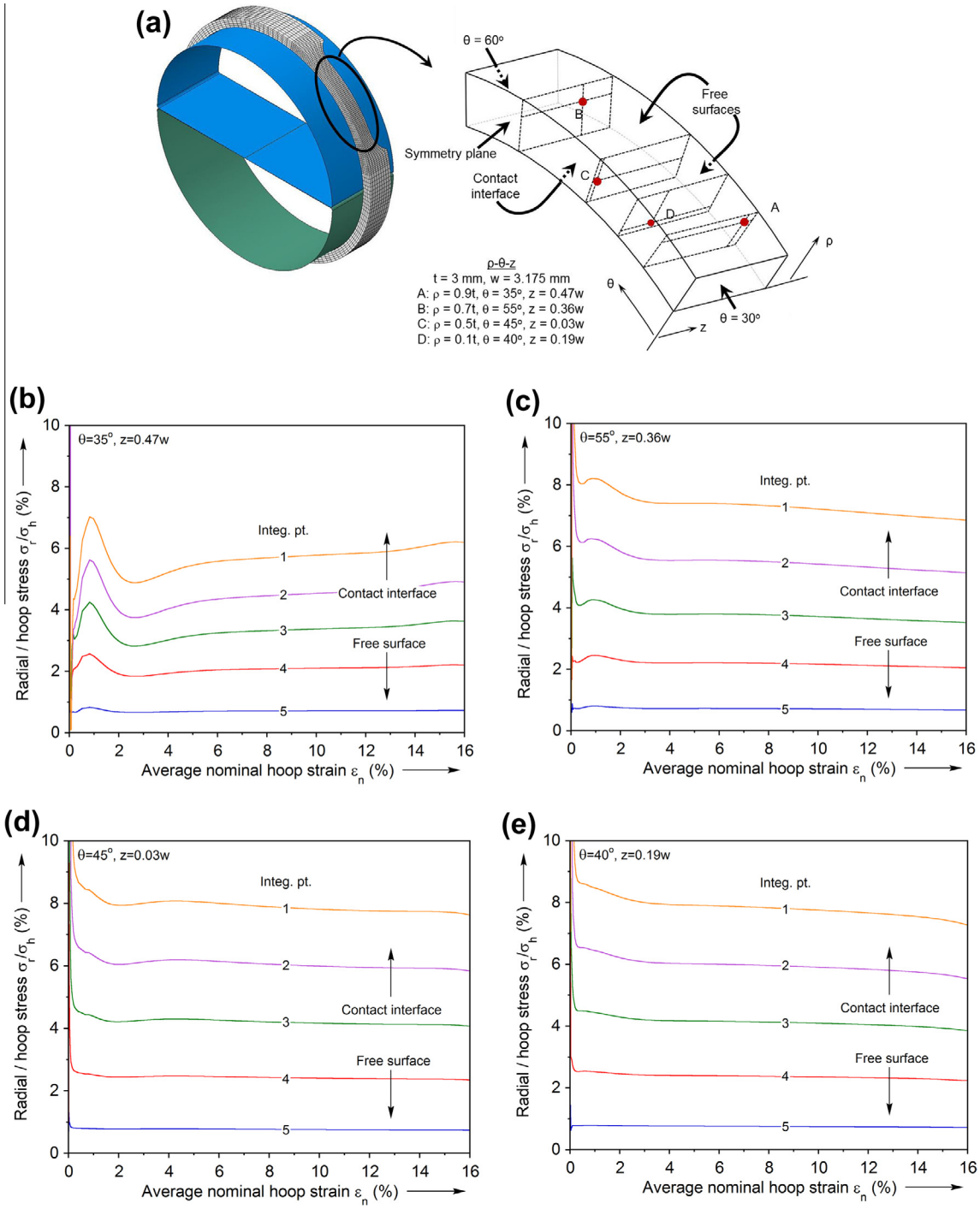

Fig. 6. (a) Output locations in the gage-section. (b–e) Radial stress normalized with the hoop stress at the 4 locations selected and at the 5 integration points at each location.

3.2. Ring Hoop Tension Tests (RHTT) on as-received material

The RHTT specimens were milled from 12.7 mm wide rings extracted from the Al-6061-T4 tubes using a lathe cut-off tool. A dogbone-shaped reduced area of 6.35 mm width was machined into the ring. The overall gage-section design followed the guidelines of the ASTM E-8 standard for subsize tension specimens (strips). Three different lengths of the gage-section were investigated here, namely 16, 24 and 35 mm (arc lengths). These corresponded to 32°, 48° and 70° arcs, as well as to 2.5, 3.8 and 5.5 length/width of the gage-section aspect ratios, respectively (see Fig. 15a). The advantage of the shorter gage length is that for any given coefficient of friction the variation of the internal hoop force is minimized (see Fig. 3). However, in such a specimen, the effect of the shoulders reduces the area where uniaxial conditions prevail. On the other hand, a longer specimen may be more affected by friction and in addition it presents correlation challenges, or even visual access, for the DIC system. Hence, in the remaining of this work we selected the 24 mm gage-section length as the best performing geometry between the two other extremes. An engineering drawing of the final specimen is given in Fig. 15b.

Two D-shaped mandrels (or D-blocks), made of hardened steel and held to clevis grips by hardened steel dowel pins were fitted inside the ring. The D-blocks were 0.5 mm undersized to the inside

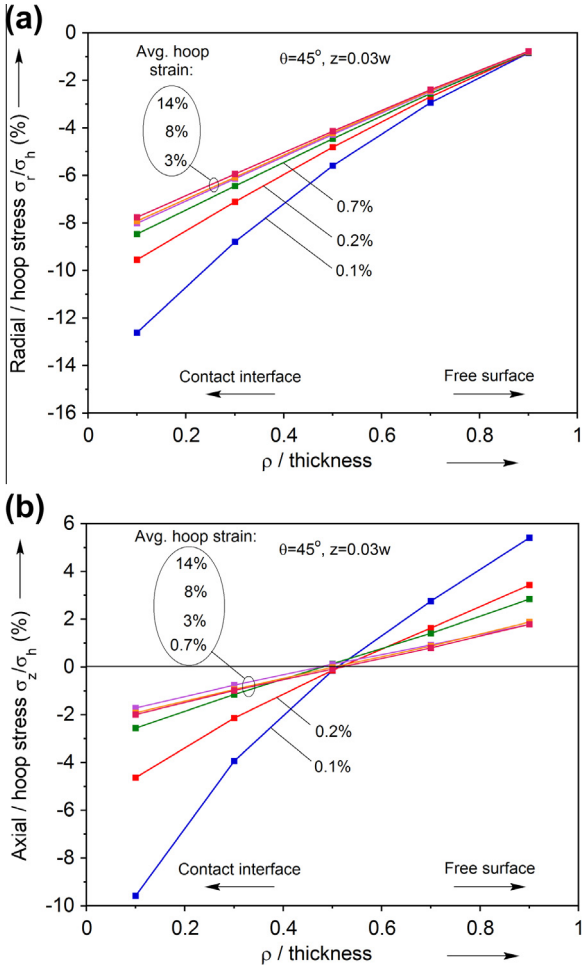

Fig. 7. (a) Variation of radial stress through the ring thickness, normalized with the corresponding hoop stress, for various levels of average hoop strain. (b) Same for the axial stress.

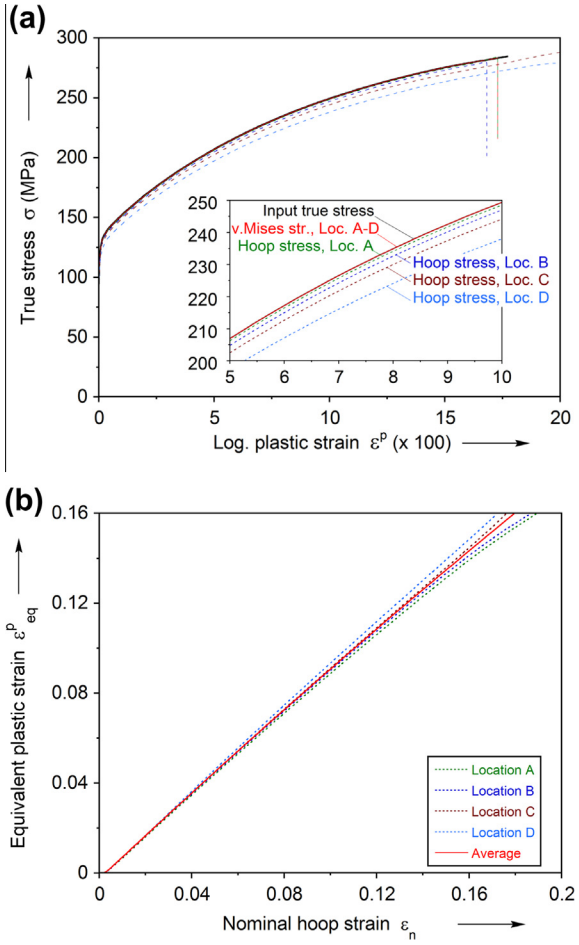

Fig. 8. (a) Finite element predictions of the hoop stress–plastic strain at the 4 locations A–D identified in Fig. 6a. Included are the input curve and the von Mises equivalent stress-equiv. plastic strain response. (b) Evolution of the vM equivalent plastic strain with the hoop strain at the same 4 locations selected.

diameter of the ring. To minimize friction, two layers of Teflon and three layers of oil were sandwiched between the ring and the D-blocks. The reduced section of the ring was placed on the D-block so that it would stay on it during the entire test and thus avoid the bending stresses (shown in Fig. 4b) that develop in the expanding gap between the D-blocks during the test. As determined from the analytical and numerical study described earlier in Section 2, the ring is then in a state of uniaxial tension throughout the test, save for the contact-induced radial and axial stresses and the friction-induced variation of the internal force.

The RHTT experiments were performed with the same testing apparatus as for the tension tests on the strips (see Fig. 16a). The displacement-rate of the actuator was set to 0.03 mm/s, calculated to induce the same strain-rate as the strip tension tests reported above. A close-up of the ring and the D-shaped mandrels is given in Fig. 16b.

The average nominal hoop stress was calculated by dividing half of the load cell reading by the average cross-sectional area, since the rings had thickness eccentricity. Furthermore, the "virtual extensometer" feature of the DIC system was used to obtain the cord of the deforming gage-section. This was then reduced to hoop nominal strain using simple geometry. The apparent (i.e., uncorrected for friction) hoop stress–strain response deduced in this way is shown in Fig. 17. Also included is the average stress–strain response determined earlier for the axial direction. The two responses are seen to differ from each other. The reasons for this

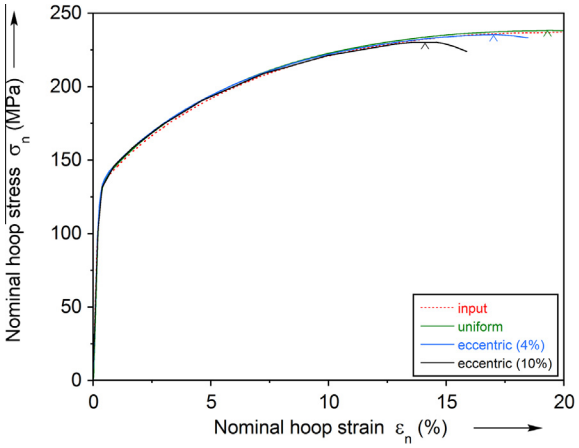

Fig. 9. Finite element prediction of the effect of thickness eccentricity on the recorded hoop stress–strain responses.

difference and the determination of whether it is due to the material anisotropy, to the testing setup, to the data reduction procedure or to a combination of these is addressed in the remaining of the paper.

The engineering hoop strain field is shown in Fig. 18a for an average nominal hoop strain of 14%. Even though there is no

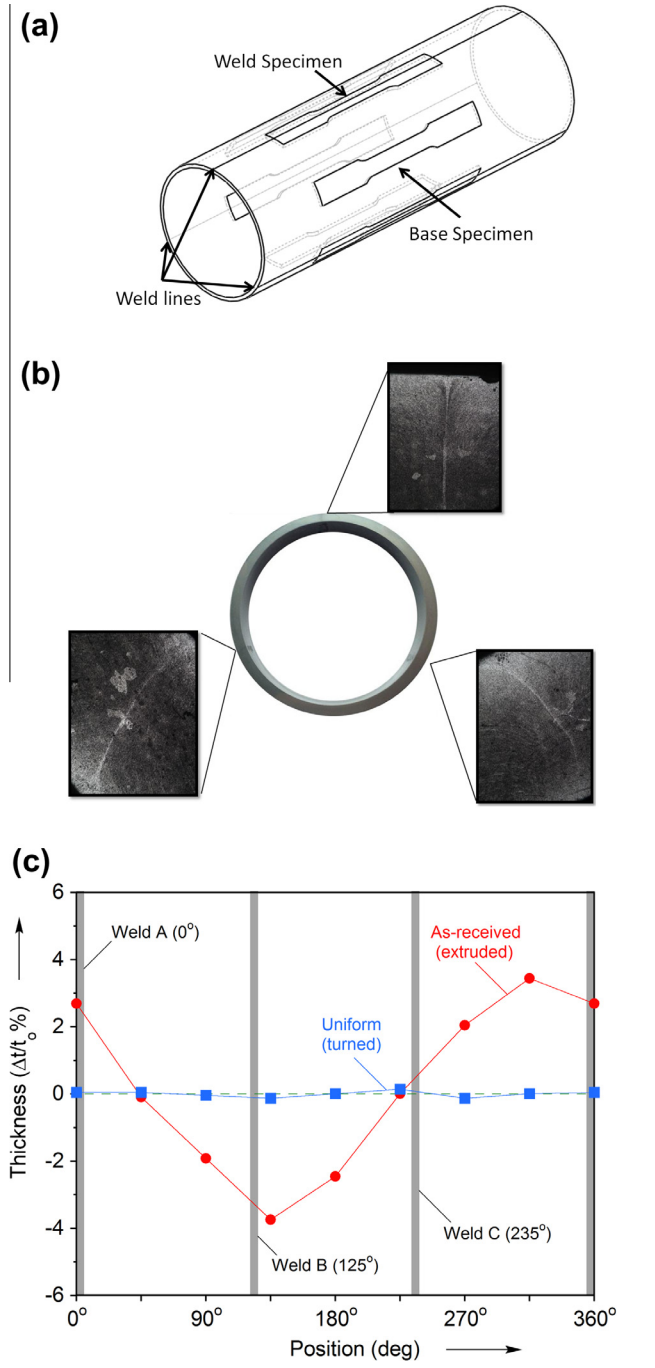

Fig. 10. (a) Locations of axial specimens extracted from the tubes. (b) Metallography of the cold-welds. (c) Tube thickness eccentricity measurements and a sketch of the tube wall thickness variation.

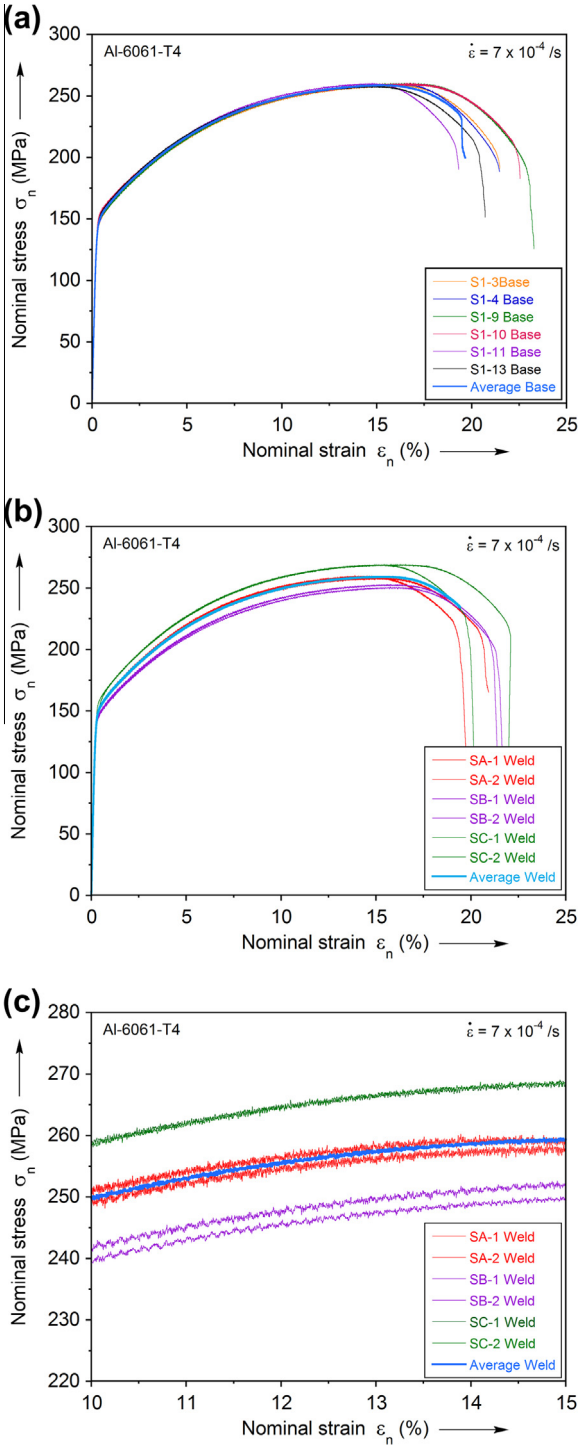

Fig. 11. (a) Axial stress–strain curves of the base material. (b) Same, for the weld material. (c) Magnification of figure (b).

obvious sign of necking, the field is non-uniform, with the top regions experiencing hoop strain of approx. 0.15 (engineering) while the middle and lower regions of the gage-section being at approx. 0.10, or 1/3 lower. This probing was repeated at various instances throughout the test, marked with green squares in Fig. 17. The results are plotted in Fig. 18b as a function of the position along the gage-section, with "zero" being at the top of the gage-section (position 1 in Fig. 18a) and "one" being at the bottom (position 9). Also included in that figure are measurements taken with calipers and a micrometer after the end of the test, to confirm the DIC results, and an inset with the initial cross-sectional area variation along the gage-section. The hoop strain is seen to be non-uniform throughout the test and certainly before necking. Notice that the local strain distribution at an average nominal strain of 14% and 17% is clearly non-uniform, while from Fig. 17, the average necking strain is over 19%. This can be explained at least partly by the thickness eccentricity of the rings (see Fig. 10c and inset in Fig. 18b): since the internal force is almost the same along the gage-section (at low coefficients of friction), the stress and hence the corresponding strain will be non-uniform. Indeed, in the particular experiment of Fig. 18b, the variation of the strain field measured agrees exactly with the thickness variation along the gage-section.

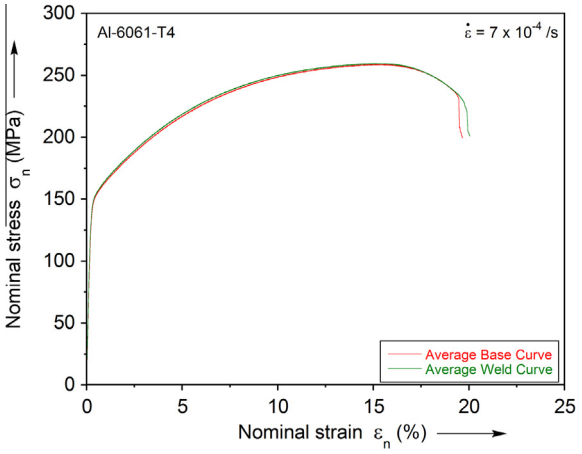

Fig. 12. Axial stress–strain curves for the base and weld material, averaged from all the experiments of the previous figure.

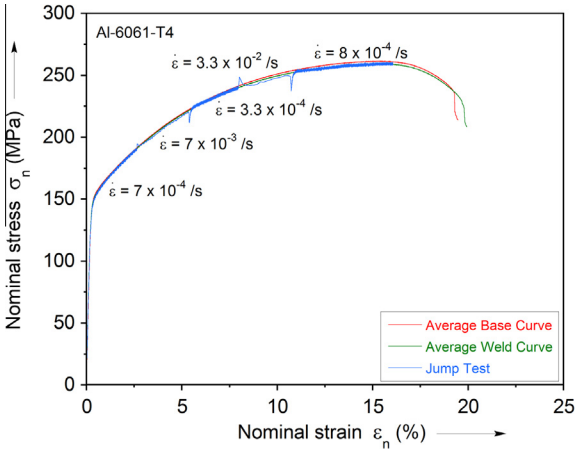

Fig. 14. Rate dependence of the base material, probed with the jump-test.

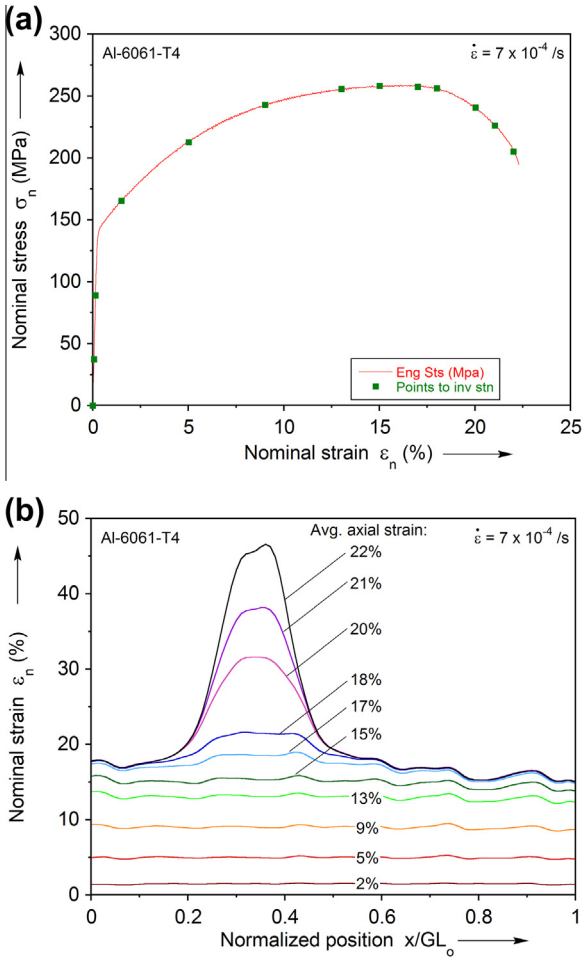

Fig. 13. (a) Points on the axial stress–strain curve to investigate with the Digital Image Correlation tool. (b) Evolution of axial strain in a tension specimen along the tube axis at the instances identified in (a), showing localization.

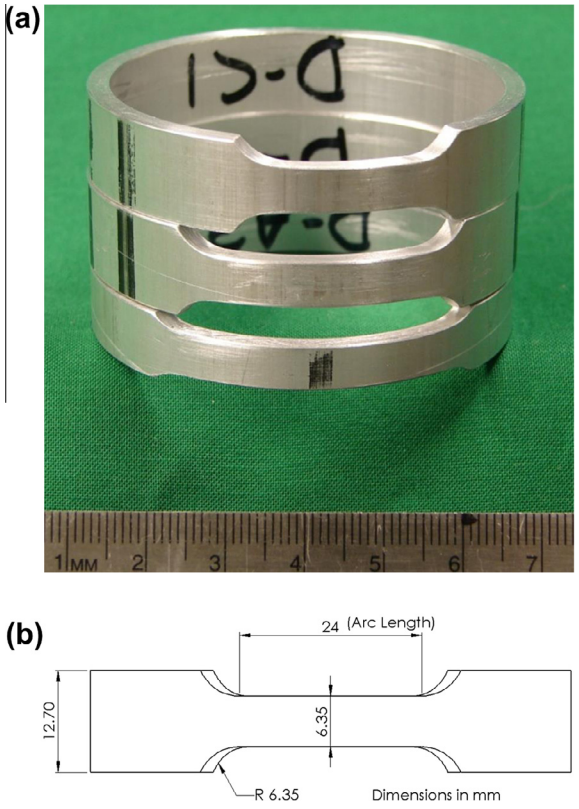

Fig. 15. (a) Some of the specimen geometries considered for the RHTT test. The one selected is the middle one. (b) Drawing of the final RHTT specimen geometry.

The DIC tool was used to further probe the response by establishing local miniature virtual extensometers along the gage-section of Fig. 18a, extracting the local hoop strain and then plotting it against the local hoop stress (i.e., the force divided by the local cross-sectional area). The results are shown in Fig. 19, along with the hoop response determined in the average sense, i.e., with the extensometer spanning the entire gage-section and the force divided with the average cross-sectional area. Also shown in Fig. 19 as an inset is the cross-sectional area variation along the gage-section. Position 2 is close to the top of the gage-section in Fig. 18a, while position 8 is close to the bottom. These positions are also identified with the black marks on the side of the gage-section in Fig. 18a. (Positions 1 and 9 are close to the shoulder region of the specimen and will not be considered here.) The local responses are seen to bundle together closely. Of course, since the thinnest sections (positions 2 and 3) experience the highest stressing, they are further ahead from the rest. At some point, deformation localizes in these sections, which experience further straining, while the responses from the rest of the specimen record

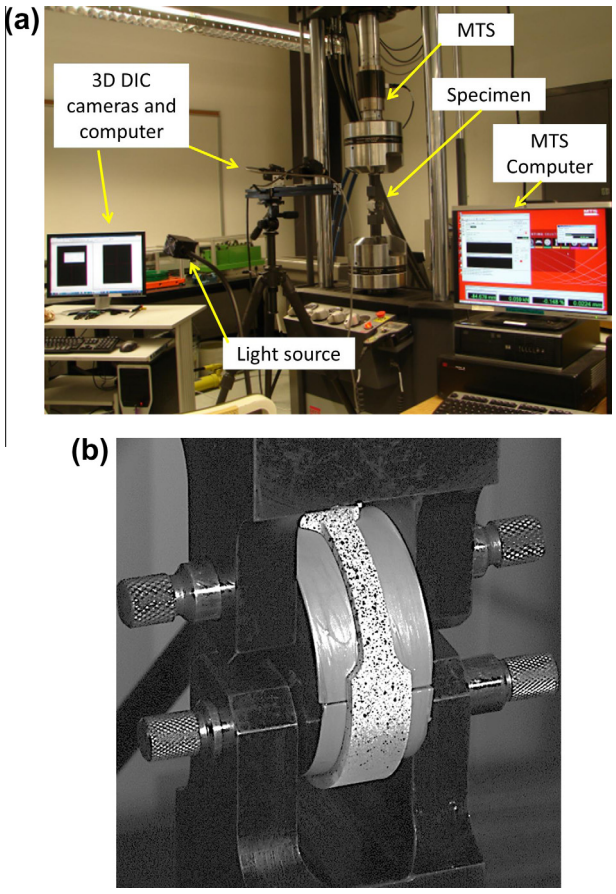

Fig. 16. (a) Test setup for the RHTT experiments. (b) Close-up of the RHTT specimen and the D-shaped mandrels.

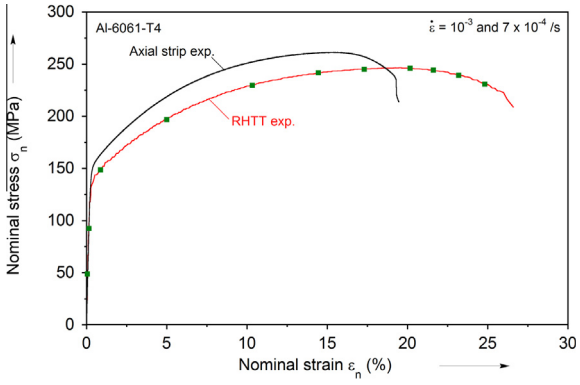

Fig. 17. Stress–strain responses in the axial and hoop directions of the tube.

elastic unloading. This is typical of a localization problem (e.g., Korkolis and Kyriakides, 2008, 2011; Giagmouris et al., 2010; Cullen and Korkolis, 2013). The average response follows the local responses closely and records a mild drop as the localization sets in. In our view, this result confirms that the RHTT is suitable for probing the material response, when care has been taken to minimize the friction between the ring and the mandrel.

The DIC strain fields were further processed to yield the Lankford coefficient or plastic strain ratio or *R*-value (Hosford and Caddell, 2007), for both the strip and the RHTT experiments. This was done by selecting 3 locations inside the gage-section (one central and two close to each end, but still within the gage-section), establishing 2 local extensometers (one in the loading

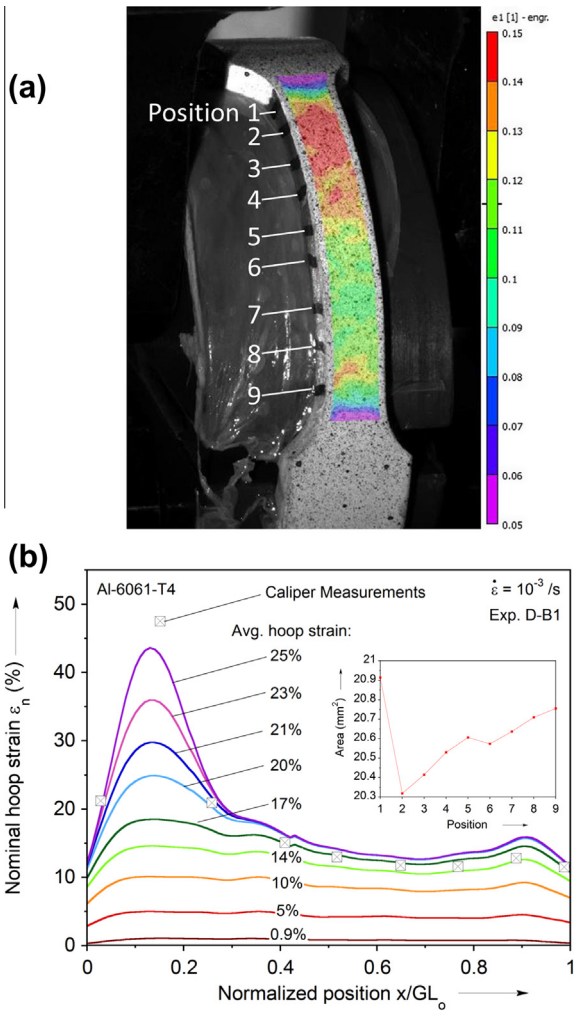

Fig. 18. (a) Lagrangian hoop strain distribution from the RHTT. (b) Evolution of the nominal hoop strain over the gage-section of the RHTT specimen. Shown as an inset is the cross-sectional area variation along the gage-section.

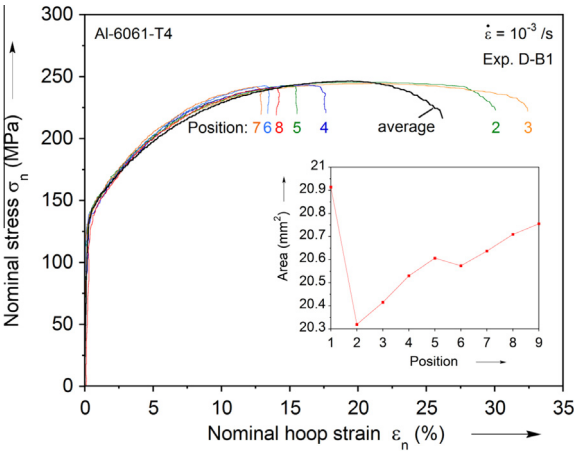

Fig. 19. Local hoop stress–strain curves. Shown as an inset is the cross-sectional area variation along the gage-section.

and one in the transverse direction) and extracting the corresponding logarithmic strains. These were converted to plastic strains and invoking incompressibility, the through-thickness plastic strain was found. The slope of the width-to-thickness plastic strain plot

was then computed for each of the 3 locations and averaged. In addition, as is often the case (Hosford and Caddell, 2007), the elastic strains were neglected and the slope of the width-to-thickness total (instead of plastic) strain plot was used for determining the *R*-value. The results for 3 specimens and the two methods are shown in Fig. 20. In the inset of Fig. 20, the directions used for each specimen type (strip and RHTT) are clarified. Note that despite the strain fields being non-uniform along the gage-section of the RHTT specimens, the corresponding *R*-values from the 3 sets of local extensometers were very close in each case (within 0.2 for either of the two RHTT specimens shown in Fig. 20). The procedure was terminated soon before the maximum load, as it requires a uniform strain field. Using the total strain ratio, the *R*-value in the axial direction (i.e., from the strip) was slightly below 1, as is often the case with aluminum alloys. However, the *R*-value in the transverse direction was approximately 2, indicating a pronounced anisotropy of the material. Using the plastic, instead of the total, strain ratio the *R*-values show a large dependence on the plastic deformation accumulated (Fig. 20). The *R*-values from the DIC strain fields were confirmed with measurements performed in the failed specimens, using digital calipers (for the width) and a digital micrometer (for the thickness). These measurements were taken away from the necked regions of the failed specimens, where the deformation has been "frozen" to the values at the onset of necking. (An error analysis of this procedure is presented in Appendix A.) The results are added in Fig. 20 and are in good agreement with the more accurate DIC measurements.

Photographs of the failed specimens from the strip tension and the RHTT experiments are shown in Fig. 21. Recall that the cross-sectional aspect ratio of both specimen geometries is identical. Also identical is the mode of failure (diffuse neck followed by rupture) in both cases, indicating that the RHTT stress field is predominantly uniaxial.

3.3. Ring Hoop Tension Tests (RHTT) on uniform/turned rings

As a further step, it was decided to remove the thickness eccentricity from the rings. This was performed by turning the extruded tubes on a lathe before the rings were extracted from them, and resulted in the reduced thickness eccentricity shown in Fig. 10c. The ±4% thickness eccentricity of the extruded tube was thus reduced to less than ±0.1%. Testing of these rings required the machining of new D-shaped mandrels, to maintain the 0.5 mm clearance between the mandrels and the ring. Indeed, when the uniform/turned rings were tested with the original mandrels, they experienced necking in two locations since the larger-than-normal clearance, however limited, led to bending and the formation of plastic hinges before the ring began to stretch. The plastic hinges led to the double necking.

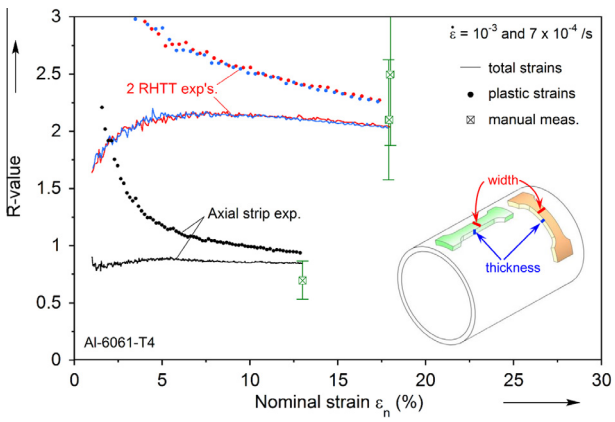

Fig. 20. Variation of the *R*-values with the accumulated plastic deformation.

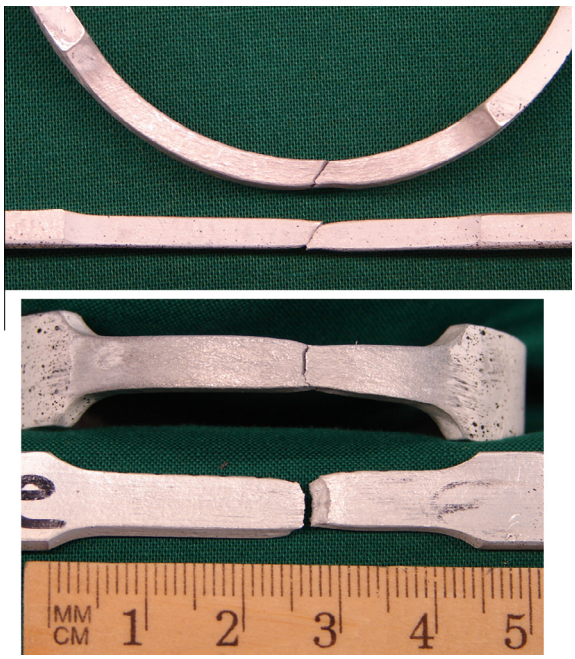

Fig. 21. Photographs of the ruptured specimens (axial and RHTT).

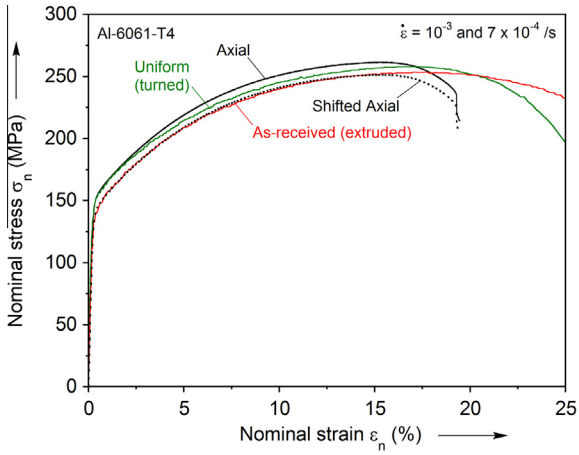

Fig. 22. Stress–strain responses recorded from the as-received (extruded) and uniform (turned) specimens. Also included are the axial response of the material and an axial response shifted vertically by 10 MPa.

The response from the uniform ring is plotted with one of the as-received (i.e., extruded) rings and the average axial response in Fig. 22. The as-received ring response has the same yield and work-hardening rate as the axial response with the stress lowered by 10 MPa. The uniform ring shows a higher yield stress and a lower work-hardening rate than the as-received one. (Notice that while specific experiments are shown in Fig. 22, these observations are representative of all experiments performed). This is surprising, in view of the fact that the numerical investigation (Fig. 9) showed no sign of the eccentricity having such an effect on the response. It must be concluded that this difference is due to factors not taken into account during the numerical modeling. Hence, the turning process must induce machining damage, as well as alter any residual stresses left over from the tube-making and the subsequent natural ageing to the T4 temper, to the extent that the behavior of Fig. 22 is observed.

To investigate the effect of machining on the response, the Al-6061-T4 tubes were heat-treated to the fully-annealed (O) state, by heating them to 420 °C, holding that temperature for 3 h and cooling in a controlled rate of 28 °C/hr. Both strips and RHTT specimens from the O-material were prepared and tested. To prevent ageing from affecting these results, the specimens were systematically tested within 18–21 h of their heat treatment cycle. The O-material nominal stress–strain responses for the axial strips and the uniform rings are shown in Fig. 23. Notice that the RHTT response is now higher than the axial one, which is the opposite of the responses shown in Fig. 22 for the T4-material. The effect of the turning process on the response was further probed by machining RHTT specimens from tubes that were first annealed and then turned, as well as from tubes that were turned and then annealed, and comparing the responses between these two families. The results shown in Fig. 24 indicate that the machining has a small but noticeable and systematic effect on the response. The trends of Fig. 24 (uniform/turned response is higher than the as-received/extruded) confirm the observations of Fig. 22.

The O-temper material was also used to further investigate the effect of eccentricity experimentally. Specimens for RHTT were prepared from as-received and uniform rings and then annealed to the O-temper and tested. The results from 6 experiments are plotted together in Fig. 25. These two families of curves fall atop one another. This further concludes that the eccentricity, at least for the levels tested in these rings, is negligible on the stress–strain response.

3.4. Establishment of the hoop stress-strain curve of the material

We now turn our attention to the establishment of the material anisotropy. The discrepancy between the axial and the hoop responses in Fig. 17 can be due to: (a) material anisotropy, (b) frictional effects, (c) geometric effects (i.e., eccentricity) and (d) specimen preparation. The latter was addressed in the preceding section. The eccentricity will be dealt with through the FEA model directly. The role of friction is now investigated with the aid of the FEA model of Section 2.2. A uniform ring with the axial stress–strain curve of the -T4 material (shown in Fig. 17) and no anisotropy was considered and compared to a RHTT experiment on a turned (i.e., uniform) ring. Since the friction causes the internal force to vary along the arc, it also causes a circumferential variation to the stress and strain fields. Then, the friction coefficient between the ring and the D-shaped mandrel was calibrated by comparing the non-uniformity of the hoop strain field recorded by the DIC (Fig. 18a and b) to

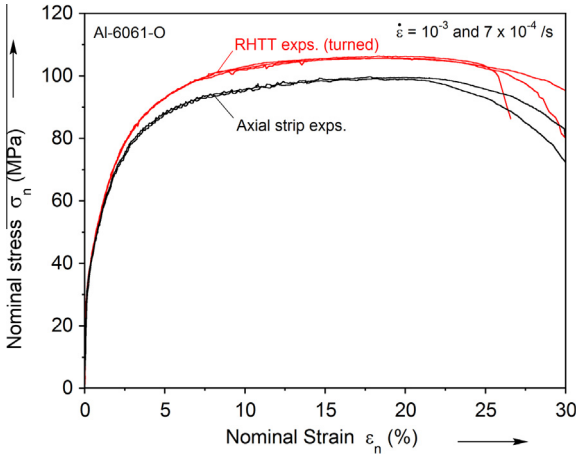

Fig. 23. Stress–strain responses in the axial and hoop directions of the annealed material. Notice that the difference between the two directions is different from the one for the -T4 material (Fig. 17).

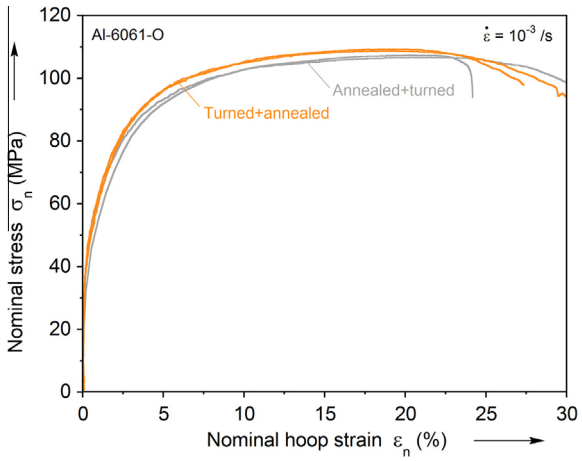

Fig. 24. Stress–strain responses from RHTT specimens of the annealed material, showing the effect of machining-induced damage.

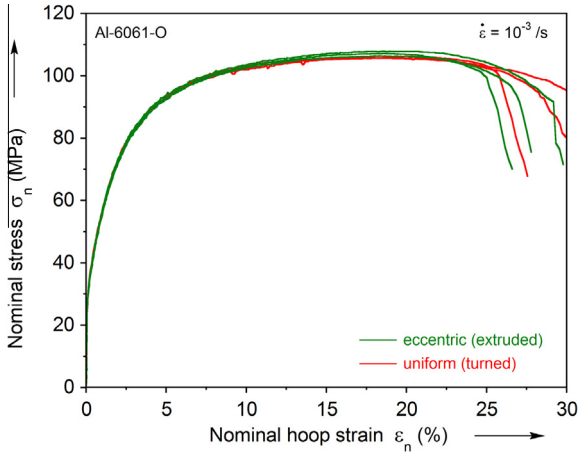

Fig. 25. Stress–strain responses from RHTT specimens of the annealed material for eccentric and uniform specimens, showing that the thickness eccentricity does not affect the response. All specimens were annealed as the final step before testing.

FEA predictions with different Coulomb coefficients. (See Korkolis and Kyriakides, 2011 for a similar approach.) The uniform ring was selected to avoid the effects of eccentricity on the hoop strain non-uniformity, leaving only friction as the cause of this variation. Notice that while the experimental result is coming from an anisotropic material and the FEA is assuming isotropy, the criterion we use for the comparison is not the absolute values of the hoop strain field but rather, the spatial variation of that field. We also assume that this variation is affected, indeed, triggered by the friction, but not by the anisotropy of the material. Hence the isotropic model can be used for this purpose.

The results are shown in Fig. 26a–c, at three levels of average hoop strain (8%, 11% and 14%). A friction coefficient of $\mu = 0.1$ offers the best agreement between experiment and analysis and will be adopted here. As can be noticed from the analytical and numerical investigation reported in Section 2, this coefficient of friction is low enough to assume that the internal force is almost uniform along the gage-section (see Fig. 3). Fig. 26a–c show that this approach is sensitive enough to distinguish the results of simulations with coefficients 0.075 and 0.125, from the optimal case of 0.1.

The procedure just described allowed the determination of friction between the ring and the D-shaped mandrel. Hence we are now ready to tackle the last reason for the axial-RHTT response discrepancy shown in Fig. 17, which is the material anisotropy.

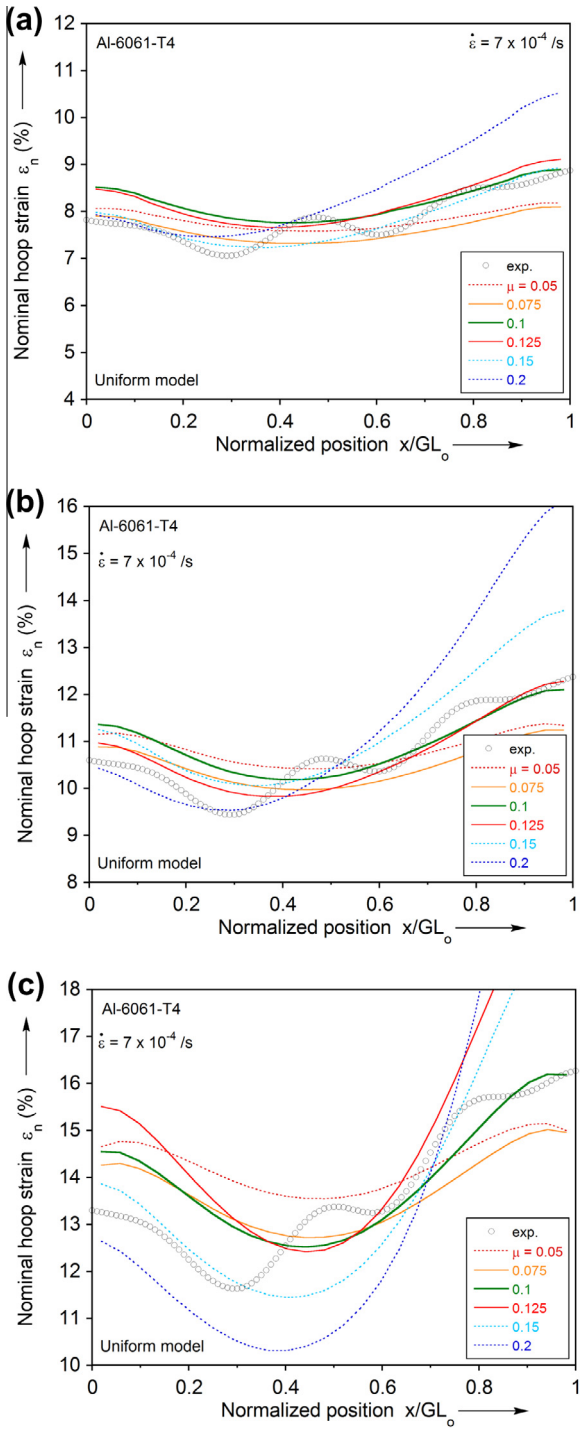

Fig. 26. Experiment and prediction of the hoop strain variation along the gage-section length. The predictions are made for different coefficients of friction listed in the figure. The comparisons are made for 3 different levels of average hoop strain: (a) 8%, (b) 11% and (c) 14%. Both experiments and simulations are for uniform thickness rings.

For this purpose, the ±4% eccentric, isotropic FEA model, including the correct friction coefficient, was compared to an eccentric RHTT experiment. Initially, using the axial stress–strain response as input to the RHTT simulation, the predicted average hoop response was found to deviate from the experimentally recorded one (see solid and dashed black curves in Fig. 27). This was expected, even after accounting for friction and geometry in our FEA model, since the material is anisotropic. Subsequently, the input stress–strain curve that was used in the RHTT simulation was iteratively adjusted manually from the axial stress–strain response (solid black curve in Fig. 27), to improve the agreement between the FEA output and the experiment. Also shown in Fig. 27 are results from an intermediate step of this process (purple). The process was repeated until the predicted hoop response of the RHTT simulation (green dashed curve in Fig. 28) matched the experimental one (red curve in Fig. 28). It was found that both the overall level and the rate-of-hardening had to be adjusted for the agreement of Fig. 28 to be possible. Since the FEA model is isotropic, the input stress–strain curve that yielded this agreement (blue curve in Fig. 28) is the same in all directions of the tube material and thus it represents the hoop response, as well. By comparing this input curve to the axial stress–strain response from the experiments (i.e., the black and blue curves in Fig. 28), the anisotropy of the actual material is established.

As a further, independent check of the validity of the hoop stress–strain response as established in Fig. 28, we employed Hill's 1948 criterion (Hosford and Caddell, 2007), calibrated from the *R*-values of Fig. 20. Note that this criterion is not suitable for describing the anisotropy of aluminum alloys, as is well established in the literature (e.g., Giagmouris et al., 2010; Korkolis and Kyriakides, 2008, 2011; Korkolis et al., 2010; Kuwabara et al., 2005; Kuwabara, 2007, among many others). However, we will only compare the responses in two selected directions (axial and hoop). Using the equation presented in Appendix B and the *R*-values of Fig. 20 (total strains), Hill's 1948 predicts that at 5% nominal strain the hoop flow stress should be 181 MPa, at 10% strain 208 MPa and at 15% strain 216 MPa. The corresponding values from the hoop stress–strain response shown in Fig. 28 are 181, 206 and 221 MPa, which are very close to the predictions. This independent check establishes the validity of the proposed procedure and of the resulting hoop stress–strain curve. Note that the use of the *R*-values derived from the plastic, instead of the total strains, yields almost identical predictions as those above.

In closing, we summarize the procedure that we propose to use for establishing the material response in the hoop direction using the Ring Hoop Tension Test. Note that this procedure generates reliable data up to the onset of necking and not necessarily beyond that.

(a) In every RHTT test, ensure that the radial clearance is kept within a tolerance (here, less than 0.5 mm) and that the friction between the D-shaped mandrel and the ring specimen is kept as low as possible, and certainly below 0.1–0.15.

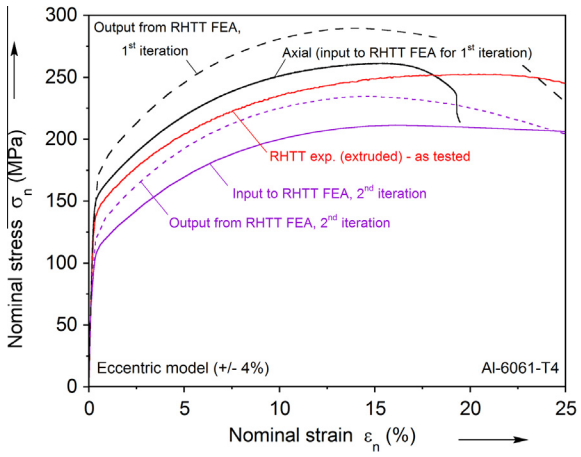

Fig. 27. Stress–strain responses in the axial and hoop directions of the T4 material, and results of simulations with the eccentric model, using different input stress–strain curves. The RHTT results are corrected for friction as described in the text. Shown are two pairs of input–output curves.

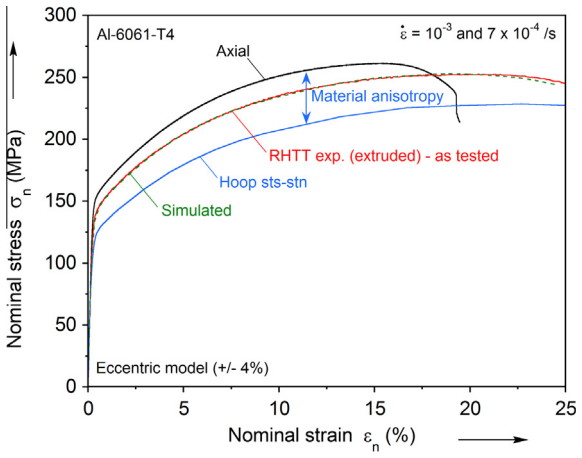

Fig. 28. Stress–strain responses in the axial and hoop directions of the T4 material. The final hoop stress–strain curve of the material is identified with light blue color. (For interpretation of the references to color in this figure legend, the reader is referred to the web version of this article.)

(b) Turning of the rings for removing the eccentricity is not necessary for determination of the average hoop stress–strain response. Furthermore, it should be avoided because of potential machining damage.

(c) The apparent hoop stress can be calculated by dividing half of the load-cell force with the average area. A mechanical or virtual (DIC) extensometer can be used for acquiring the hoop strain. The resulting curve is not the material behavior in the hoop direction, because it has to be corrected for friction (which is why we refer to this hoop stress as "apparent").

(d) To calibrate the friction, the full strain field in the hoop direction should be available, either during the test or even only at the end of it. Then, by comparing the predictions of an isotropic FEA model to the experimental strain field, the Coulomb friction coefficient can be determined. In case of using DIC, attention must be paid to the speckle pattern and the data reduction, to avoid the waviness shown in Fig. 26a–c as much as possible.

(e) After calibrating the friction, the isotropic FEA model can be used to determine the hoop stress–strain curve of the material by starting with the axial stress–strain curve and modifying it, until the FEA-predicted average hoop response matches the experimentally recorded (determined in step (c) above). The input curve that yields that behavior is the hoop stress–strain curve of the material. Comparing that curve to the axial stress–strain response (i.e., from the strip tension tests) establishes the anisotropy of the material.

Note that while we have countered for all other factors in the RHTT, the present framework cannot distinguish between the effect of the initial anisotropy and the residual stresses in the recorded response. While for the tubes examined here we anticipate that the natural ageing process has left little residual stresses, this will not be the case for other materials/tempers.

4. Conclusions and future work

To assess the hoop response of tubular materials, the Ring Hoop Tension Test (RHTT) was examined in detail. A very simple analytical model was examined first, to highlight the effect of friction on the internal force distribution. A finite element model of RHTT was then constructed and used to probe the uniformity of the hoop stress in the gage-section, the magnitude of the contact pressure between the ring and the D-shaped mandrel and the magnitude of the contact-induced radial and axial stresses. It was concluded that these effects are comparable to those induced by the internal pressure in the tube inflation experiments. Also assessed was the effect of the thickness eccentricity on the response, which was found to be negligible even for this relatively large thickness eccentricity. It was determined that in every case, as long as the tube-mandrel friction is kept at a low value, the RHTT can be used to assess the hoop response of the material.

The experiments reported here involved extruded Al-6061-T4 tubes. The axial properties were first assessed by extracting and testing specimens in the axial direction of the tubes. An abrupt-strain-rate-change-, or jump-test was performed to assess the strain-rate dependence of the material, which was found to be negligible for the rates considered here (7×10^{-4} to 3.3×10^{-2}/s). Subsequently, RHTT experiments were performed. Three specimen geometries were considered. The average apparent hoop stress was calculated by dividing half of the load cell reading by the average cross-sectional area. A Digital Image Correlation system was used to assess the full strain field and its evolution during RHTT, as well as to provide the average hoop strain. It was discovered that the hoop strain was non-uniform throughout the test. This was explained by the thickness eccentricity of the rings. Miniature local virtual extensometers were established along the gage-section and the local hoop stress–strain responses were determined. These responses agreed quite well with each other, until necking occurred.

The average apparent hoop stress–strain response (i.e., uncorrected for friction) was found to be different from the axial response of the material. Subsequently, uniform/turned rings were tested and found to follow a different response from either of the previous two. This was determined to be due to machining and specimen-making damage, by testing heat-treated (fully annealed) specimens. Hence the benefit of uniform thickness was negated by inducing machining damage to the material. The ring-mandrel friction coefficient was calibrated by using the finite element model. Then, the input curve to this model was adjusted so that the predicted hoop response matched the experimental one. The adjustment involved both the overall level and the rate-of-hardening. This input curve is the stress–strain response of the material in the hoop direction. A step-by-step description of the proposed testing method for assessing the hoop properties of materials in tubular form is given at the end of Section 3.4.

Finally, the results presented here refer to a relatively thick-walled tube. It is anticipated that any deviations of the RHTT from pure uniaxial tension in the hoop direction, save for the effects of tube-mandrel friction, will be milder when testing thinner tubes.

Acknowledgments

This work was performed under the GOALI Grant CMMI 1031169 from the National Science Foundation, whose support is acknowledged with thanks. The tubes were provided by Dr. Cedric Xia from Ford Motor Company. We thank Adam Kaplan for preliminary experimental work in this area and Alex Roy for help with machining of the specimens. We also acknowledge helpful discussions with Prof. Todd Gross at UNH. Finally, we would like to acknowledge the feedback from the anonymous reviewers who helped us improve the content and presentation of this work.

Appendix A

In this appendix, we calculate the uncertainty expected in the caliper/micrometer measurements of the *R*-values, shown in Fig. 20. These refer to the total strains. Since:

$$R = \frac{\varepsilon_w}{\varepsilon_t} = \frac{ln\frac{w}{w_o}}{ln\frac{t}{t_o}} \tag{A.1}$$

The uncertainty is:

$$u_R = \sqrt{\left(\frac{\partial R}{\partial w}u_w\right)^2 + \left(\frac{\partial R}{\partial w_0}u_w\right)^2 + \left(\frac{\partial R}{\partial t}u_t\right)^2 + \left(\frac{\partial R}{\partial t_0}u_t\right)^2} \tag{A.2}$$

After some algebra, this reduces to:

$$u_R = \frac{1}{\varepsilon_t}\sqrt{\left(\frac{1}{w^2}+\frac{1}{w_o^2}\right)u_w^2 + R^2\left(\frac{1}{t^2}+\frac{1}{t_o^2}\right)u_t^2} \tag{A.2}$$

Using the values relevant to the undeformed and deformed to 15% nominal strain specimens, and assuming the uncertainty of the width and thickness measurements to be 3% (a reasonable estimate in our experience), we find that for the strip specimen $u_R/R = 23.9\%$ while for RHTT specimen $u_R/R = 25.1\%$. These are the error bars shown in Fig. 20.

Appendix B

For the case that the principal loading directions coincide with the principal anisotropic axes of a material, the Hill 1948 criterion can be written in terms of the R-values in two perpendicular directions (e.g., for a tube, axial and hoop or 0° and 90°) as (Hosford and Caddell, 2007):

$$R_0\sigma_{90}^2 + R_{90}\sigma_0^2 + R_0R_{90}(\sigma_0 - \sigma_{90})^2 = R_{90}(1+R_0)\sigma_{Y,0}^2 \tag{B.1}$$

Then, in the case of loading in the hoop direction, the criterion predicts:

$$\sigma_{90} = \sqrt{\frac{R_0}{R_{90}}\frac{1+R_{90}}{1+R_0}}\,\sigma_{Y,0} \tag{B.2}$$

Note that as explained in the text, the Hill 1948 criterion is only used to compare 2 directions (axial and hoop). It is not proposed as a suitable criterion to describe the orthotropy of this aluminum alloy (Giagmouris et al., 2010; Korkolis and Kyriakides, 2008, 2011; Korkolis et al., 2010; Kuwabara et al., 2005; Kuwabara, 2007).

References

Anon. (2012). Abaqus Ver. 6.12 Documentation, Simulia Central.

Arsene, S., Bai, J., 1996. A new approach to measuring transverse properties of structural tubing by a ring test. J. Test. Eval. 24, 386–391.

Arsene, S., Bai, J., 1998. A new approach to measuring transverse properties of structural tubing by a ring test – experimental investigation. J. Test. Eval. 26, 26–30.

ASTM, 2008. E8/E8M: Standard Test Methods for Tension Testing of Metallic Materials. American Society for Testing Materials, Annual Book of ASTM Standards, PA, USA.

Cullen, G.W., Korkolis, Y.P., 2013. Ductility of 304 stainless steel under pulsed loading. Int. J. Solids Struct. 50, 1621–1633.

Daxner, T., Rammerstorfer, F.G., Fischer, F.D., 2005. Instability phenomena during the conical expansion of circular cylindrical shells. Comput. Methods Appl. Mech. Eng. 194, 2591–2603.

Dick, C.P., 2014. Tube formability and pulsed tube hydroforming (MS thesis). UNH.

Giagmouris, T., Kyriakides, S., Korkolis, Y.P., Lee, L.-H., 2010. On the localization and failure in aluminum shells due to crushing-induced bending and tension. Int. J. Solids Struct. 47, 2680–2692.

He, Z.B., Yuan, S.J., Liu, G., Wu, J., Cha, W.W., 2008. Force and deformation analysis of tube ring specimen during hoop tension test. Acta Metall. Sin. 44, 423–427.

He, Z.B., Yuan, S.J., Liu, G., Wu, J., Cha, W.W., 2010. Formability testing of AZ31B magnesium alloy tube at elevated temperature. J. Mater. Proc. Technol. 210, 877–884.

Hosford, W.F., Caddell, R.M., 2007. Metal Forming: Mechanics and Metallurgy. Cambridge Univ. Press, New York, NY.

Kachanov, L.M., 2004. Fundamentals of the Theory of Plasticity. Dover Publ, New York.

Kim, J.H., Korkolis, Y.P., Lee, M.G., accepted for publication. Recent developments in hydroforming technology. P. I. Mech. Eng. B-J. Eng.

Korkolis, Y.P., Kyriakides, S., 2008. Inflation and burst of anisotropic aluminum tubes for hydroforming applications. Int. J. Plast. 24 (3), 509–543.

Korkolis, Y.P., Kyriakides, S., 2009. Path-dependent failure of inflated aluminum tubes. Int. J. Plast. 25 (11), 2059–2080.

Korkolis, Y.P., Kyriakides, S., 2011. Hydroforming of anisotropic aluminum tubes. Part II: analysis. Int. J. Mech. Sci. 53, 83–90.

Korkolis, Y.P., Kyriakides, S., Giagmouris, T., Lee, L.-H., 2010. Constitutive modeling and rupture predictions of Al-6061-T6 tubes under biaxial loading paths. J. Appl. Mech. ASME 77, 064501-1–0645015.

Korkolis, Y.P., Dick, C.P., Kaplan, A.R., Kinsey, B.L., 2013. Formability assessment of Al-6xxx-T4 tubes for hydroforming applications. In: SAE World Congress, Detroit, MI.

Kuwabara, T., 2007. Advances in experiments on metal sheets and tubes in support of constitutive modeling and forming simulations. Int. J. Plast. 23, 385–419.

Kuwabara, T., Sugawara, F., 2013. Multiaxial tube expansion test method for measurement of sheet metal deformation behavior under biaxial tension for a large strain range. Int. J. Plast. 45, 103–118.

Kuwabara, T., Yoshida, K., Narihara, K., Takahashi, S., 2005. Anisotropic plastic deformation of extruded aluminum alloy tube under axial forces and internal pressure. Int. J. Plast. 21, 101–117.

Kuwabara, T., Hashimoto, K., Iizuka, E., Yoon, J.W., 2011. Effect of anisotropic yield functions on the accuracy of hole expansion simulations. J. Mater. Process. Technol. 211, 475–481.

Lange, K. (Ed.), 1985. Handbook of Metal Forming. Soc. of Manufacturing Engineers, Dearborn, MI.

Link, T.M., Koss, D.A., Motta, A.T., 1998. Failure of Zircalloy cladding under transverse plane-strain deformation. Nucl. Eng. Des. 186, 379–394.

Walsh, E.J., Adams, D.O., 2008. Development and evaluation of the quadrant ring test method. Exp. Mech. 48, 319–326.

Wang, H., Bouchard, R., Eagleson, R., Martin, P., Tyson, W.R., 2002. Ring hoop tension test (RHTT): a test for transverse tensile properties of tubular materials. J. Test. Eval. 30, 382–391.